Comparison of the absolute nodal coordinate and geometrically exact formulations for beams*

Olivier A. Bauchau and Shilei Han
University of Michigan-Shanghai Jiao Tong University Joint Institute
Shanghai, 200240, China
Aki Mikkola and Marko K. Matikainen
Department of Mechanical Engineering
Lappeenranta University of Technology
Skinnarilankatu 34,
SF-53851 Lappeenranta, Finland

July 12, 2015

Abstract

The modeling of flexibility in multibody systems has received increase scrutiny in recent years. The use of finite element techniques is becoming more prevalent, although the formulation of structural elements must be modified to accommodate the large displacements and rotations that characterize multibody systems. Two formulations have emerged that have the potential of handling all the complexities found in these systems: the absolute nodal coordinate formulation and the geometrically exact formulation. Both approaches have been used to formulate naturally curved and twisted beams, plate, and shells. After a brief review of the two formulations, this paper presents a detailed comparison between these two approaches; a simple planar beam problem is examined using both kinematic and static solution procedures. In the kinematic solution, the exact nodal displacements are prescribed and the predicted displacement and strain fields inside the element are compared for the two methods. The accuracies of the predicted strain fields are found to differ: the predictions of the geometrically exact formulation are more accurate than those of the absolute nodal coordinate formulation. For the static solution, the principle of virtual work is used to determine the solution of the problem. For the geometrically exact formulation, the predictions of the static solution are more accurate than those obtained from the kinematic solution; in contrast, the same order of accuracy is obtained for the two solution procedures when using the absolute nodal coordinate formulation. It appears that the kinematic description of structural problems offered by the absolute nodal coordinate formulation leads to inherently lower accuracy predictions than those provided by the geometrically exact formulation. These observations provide a rational for explaining why the absolute nodal coordinate formulation computationally intensive.

1 Introduction

Eberhard and Schiehlen [1] have presented an extensive review of the many formalisms that have been introduced for the dynamic analysis of multibody systems. Often, the system bodies are assumed to be rigid, which may be an acceptable assumption for the analysis of motion and forces

* *Multibody System Dynamics*, **32**(1): pp 67-85, 2014

in many practical engineering problems. In other cases, however, effects of deformation should be included in the analysis to improve the accuracy of the predictions, and numerous approaches have been proposed to describe the kinematics of the problem. In the simplest approaches, deformations are assumed to remain small, leading to the use of linear strain-displacement and stress-strain relationships. For other applications, the deformation of a body may affect the system's dynamic response, calling for the use of advanced modeling techniques involving nonlinear strain-displacement relationships, or constitutive laws, or both. Wasfy and Noor [2] presented a comprehensive review of these mathematical models that can account for both material and geometric nonlinearities.

It is not uncommon for multibody systems to comprise bodies subjected to varying levels of deformation. Accordingly, rigid bodies or elastic bodies undergoing small deformations can be modeled using rigid-body dynamics or floating frame of reference [3, 4, 5] formulations, respectively. For bodies undergoing large displacements and rotations but small deformations, nonlinear strain-displacement relationships must be used, as is the case in the geometrically exact formulation [6] or absolute nodal coordinate formulation [7]. Alternatively, the co-rotational formulation could be used; in that case, linear strain-displacement relationships are used, but the element frame must handle large displacements and rotations. Finally, if deformations become large, nonlinear constitutive laws must complement the nonlinear strain-displacement relationships [8].

Consequently, the finite element method has found increasing use in the analysis of flexible multibody systems; the textbook of Géradin and Cardona [9] is devoted to this topic. One of the hallmarks of this approach is its versatility: structures of arbitrary topology can be modeled easily. This important feature is achieved by using a unified kinematic representation for all elements. Models of the complete system are then obtained through a straightforward Boolean assembly process [10, 11].

Simo and Vu-Quoc [6, 12] developed the *geometrically exact beam formulation* (GEBF), which is based on nodal displacement and rotation coordinates. This formulation is applicable to both beams and plates, and is based on finite, rather than infinitesimal rotations, allowing the exact description of rigid-body motions of arbitrary magnitudes. The displacement and rotation fields are interpolated independently, based on their nodal values, enabling the representation of transverse shear deformations. Although the two fields are interpolated independently, both are coupled through elastic forces. The kinematics of geometrically beams was first presented by Simo *et al.* [12], but similar developments were proposed by Borri and Merlini [13] or Danielson and Hodges [14, 15].

In the *absolute nodal coordinate formulation* (ANCF) developed by Shabana *et al.* [7], the shape function matrix and the vector of nodal coordinates can represent arbitrary large rigid-body motions exactly. Rotational coordinates are eliminated [16] because independent global slopes, which are partial derivatives of the position vector with respect to the element coordinates, describe the element orientation. This particular feature of the absolute nodal coordinate formulation causes the mass matrix to become constant for two- and three-dimensional elements, resulting in a particularly simple form of the equations of motion. A number of beam and plate elements have been developed based on the absolute nodal coordinate formulation.

The objective of this paper is to compare the two aforementioned formulations. For simple problems, Romero [17] showed that the absolute nodal coordinate and geometrically exact formulations do not always converge to the same numerical solution if elastic forces are defined using a continuum mechanics approach in the ANCF. He concluded that the absolute nodal coordinate formulation typically requires more computational effort, but the development of the formulation is more straightforward. Unfortunately, the absolute nodal coordinate formulation suffers from a number of locking mechanisms that must be eliminated to obtain accurate results. As pointed out by Gerstmayr *et al.* [8], this can be accomplished in a number of ways, but the proposed techniques complicate the description of elastic forces, leading to more arduous implementations and moving away from the simplicity of the initial implementation.

Romero concluded that the absolute nodal coordinate formulation is more computationally

intensive than the geometrically exact formulations. Despite the number of comparative studies that have been performed, it is still unclear why the ANCF requires more computational effort than the GEBF. This paper details the differences between the absolute nodal coordinate formulation and the geometrically exact beam formulation, and explains why the absolute nodal formulation is computationally intensive.

2 Formulation of beam elements

In Euler-Bernoulli beam and Kirchhoff plate formulations, transverse shear strains are assumed to vanish and hence, rotation of the cross-sectional plane and of the normal material line, respectively, are obtained from derivatives of the displacement field, and curvatures are expressed in terms of second derivatives of the same field [18]. In contrast, shear deformable beams and plates, often called Timoshenko beams [19, 20] and Reissner-Mindlin plates [21, 22], respectively, are Cosserat solids: the kinematics of these structural components are described in terms of two independent fields, a displacement field and a rotation field. Reissner investigated beam theory for large strains [23] and large displacements of spatially curved members [24, 25].

In two- and three-dimensional elasticity, the rotation field is not independent of the displacement field. Indeed, the polar decomposition theorem can be used to decompose the deformation gradient tensor into a stretch tensor and an orthogonal rotation tensor [26]. Because this decomposition is unique, the deformation gradient tensor, a function of the displacement field only, defines the rotation field unambiguously. This contrasts with Cosserat solids for which the displacement and rotation fields are independent.

A beam is defined as a structure having one of its dimensions much larger than the other two, as depicted in fig. 1. The axis, or reference line, of the beam is defined along that longer dimension and its cross-section is normal to this axis. The cross-section's geometric and physical properties are assumed to vary smoothly along the beam's span.

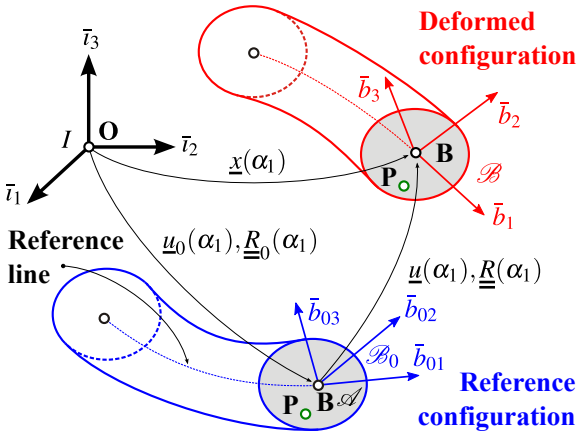

Figure 1: Curved beam in the reference and deformed configurations.

Figure 1 depicts an initially curved and twisted beam of length L, with a cross-section of arbitrary shape and area $\mathcal{A}$. The volume of the beam is generated by sliding the cross-section along the reference line of the beam, which is defined by an arbitrary curve in space. Curvilinear coordinate α_1 defines the intrinsic parameterization of this curve, *i.e.*, it measures length along the beam's reference line. Point **B** is located at the intersection of the reference line with the plane of the cross-section.

2.1 Kinematics of the problem

In the reference configuration, an orthonormal basis, $\mathcal{B}_0(\alpha_1) = (\bar{b}_{01}, \bar{b}_{02}, \bar{b}_{03})$, is defined at point **B**. Vector $\bar{b}_{01}$ is the unit tangent vector to the reference curve at that point, and unit vectors $\bar{b}_{02}$ and $\bar{b}_{03}$ define the plane to the cross-section. An inertial reference frame, $\mathcal{F}_I = [\mathbf{O}, \mathcal{I} = (\bar{\imath}_1, \bar{\imath}_2, \bar{\imath}_3)]$, is defined, and the components of the rotation tensor that brings basis $\mathcal{I}$ to $\mathcal{B}_0$, resolved in basis $\mathcal{I}$, are denoted $\underline{\underline{R}}_0(\alpha_1)$.

The position vector of point **B** along the beam's reference line is denoted $\underline{u}_0(\alpha_1)$. The position vector of material point **P** of the beam then becomes $\underline{x}(\alpha_1, \alpha_2, \alpha_3) = \underline{u}_0(\alpha_1) + \alpha_2\, \bar{b}_{02} + \alpha_3\, \bar{b}_{03}$, where α_2 and α_3 are the material coordinates along unit vectors $\bar{b}_{02}$ and $\bar{b}_{03}$, respectively. Coordinates α_1, α_2, and α_3 form a natural choice of coordinates to represent the configuration of the beam.

In the deformed configuration, all the material points located on a cross-section of the beam move to new positions. This motion is decomposed into two parts, a rigid-body motion and a warping displacement field. The rigid-body motion consists of a translation of the cross-section, characterized by displacement vector $\underline{u}(\alpha_1)$ of reference point **B**, and of a rotation of the cross-section, which brings basis $\mathcal{B}_0$ to $\mathcal{B}(\alpha_1) = (\bar{b}_1, \bar{b}_2, \bar{b}_3)$, see fig. 1. The components of the position vector of point **B** in the deformed configuration is denoted $\underline{x}(\alpha_1)$ and the components of the rotation tensor that brings basis $\mathcal{B}_0$ to $\mathcal{B}$ are denoted $\underline{\underline{R}}(\alpha_1)$; all tensor components are resolved in basis $\mathcal{I}$.

For shear deformable beams, the deformation is characterized by six sectional strains: the axial strain, the two transverse shear strains, the twist rate, and the two bending curvatures. Of course, for Euler-Bernoulli beams, the two transverse shear strains are assumed to vanish. As described in the following section, the evaluation of these sectional strains differs in the ANCF and GEBF.

Because the examples to be presented in this paper deal with planar problems, the discussion will be limited to planar kinematics, as shown in fig. 2. In this case, three of the sectional strain components vanish, leaving three non-vanishing components only: the curvature, κ, the axial strain ϵ, and the transverse shear strain, γ. Of course, the last strain component, γ, is assumed to vanish in the ANCF.

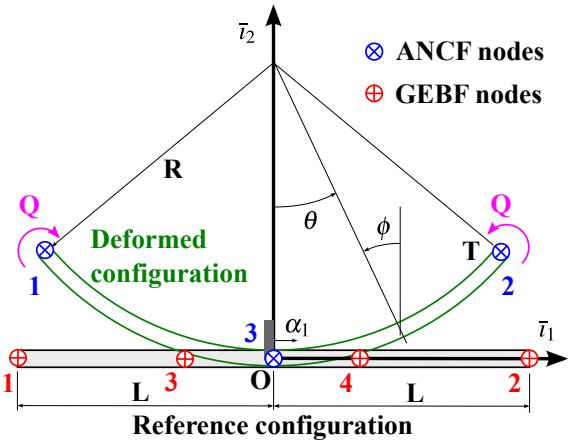

Figure 2: Planar deformation of a beam. For clarity of the figure, the GEBF and ANCF nodes are shown on the reference and deformed configurations of the beam, respectively.

2.2 Strain definition and interpolation technique for ANCF

In the ANCF, the curvature is expressed in terms of the position vector of the beam's reference line [27] as

$$\kappa = \frac{x_1' x_2'' - x_2' x_1''}{\|\underline{x}'\|^2}, \tag{1}$$

where subscripts refer to vector component and notation $(\cdot)'$ indicates a derivative with respect to curvilinear variable α_1, see fig. 1. Note that the first and second derivatives of the position vector appear in this expression, which is valid for planar problems only. The axial strain field is expressed in terms of the first derivative of the same position vector

$$\varepsilon = \frac{1}{2}\left(\|\underline{x}'\|^2 - 1\right). \tag{2}$$

In this approach, the shear strain is assumed to vanish, *i.e.*, $\gamma = 0$. Note that the ANCF does not require a description of the cross-sectional rotation field because this rotation angle can be obtained from the orientation of the tangent to the beam's reference line.

In the ANCF, the interpolation of the position field takes the following form,

$$\underline{x}(s) = h_1(s)\underline{\hat{x}}^{(1)} + h_2(s)\underline{\hat{r}}^{(1)} + h_3(s)\underline{\hat{x}}^{(2)} + h_4(s)\underline{\hat{r}}^{(2)}, \tag{3}$$

where $s \in [-1, +1]$ is a non-dimensional variable along the span of the element, as indicated in fig. 3. Notation $\hat{(\cdot)}^{(i)}$ indicates the value of a quantity at node i. The interpolation is based on the nodal values of the position vector, denoted $\underline{\hat{x}}^{(1)}$ and $\underline{\hat{x}}^{(2)}$, at node 1 and 2, respectively, and on the first derivatives, or slopes, of the same vector, denoted $\underline{\hat{r}}^{(1)}$ and $\underline{\hat{r}}^{(2)}$, at node 1 and 2, respectively. The shape functions of the element are defined as follows [28, 29],

$$\begin{aligned} h_1(s) &= \frac{1}{4}(s-1)^2(s+2), \quad & h_3(s) &= -\frac{1}{4}(s+1)^2(s-2), \\ h_2(s) &= \frac{1}{4}(s-1)^2(s+1), \quad & h_4(s) &= \frac{1}{4}(s+1)^2(s-1). \end{aligned} \tag{4}$$

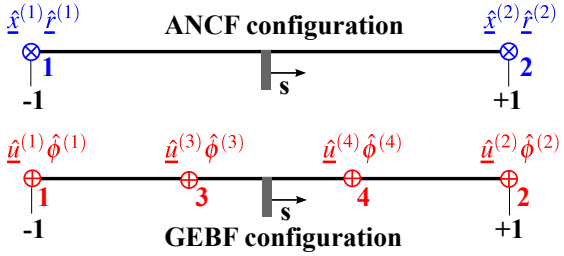

Figure 3: Element configuration for ANCF and GEBF.

2.3 Strain definition and interpolation technique for GEBF

In the GEBF, the geometry of the beam is described by the displacement field of the beam's reference axis and by the rotation field of its cross-section; for a planar problem this rotation tensor reduces to

$$\underline{\underline{R}} = \begin{bmatrix} \cos\phi & -\sin\phi & 0 \\ \sin\phi & \cos\phi & 0 \\ 0 & 0 & 1 \end{bmatrix}, \tag{5}$$

where ϕ is the cross-section's rotation angle, see fig. 2. Note that for the circular bending illustrated in the figure, angles ϕ and θ are equal; in general, however, these two angles are distinct.

The curvature field is expressed as

$$\underline{\kappa}(\alpha_1) = \text{axial}(\underline{\underline{R}}'\underline{\underline{R}}^T). \tag{6}$$

For the planar problem under investigation, the curvature vector has a single non-vanishing component,

$$\kappa = \frac{\mathrm{d}\phi}{\mathrm{d}\alpha_1} = \frac{1}{\varrho}, \tag{7}$$

where ϱ the radius of curvature, as indicated in fig. 3. For convenience, the non-dimensional radius of curvature and curvature are defined as

$$\bar{\varrho} = \frac{\varrho}{L}; \quad \text{and} \quad \bar{\kappa} = \frac{L}{\varrho}, \tag{8}$$

respectively.

The strain field is defined as

$$\underline{\varepsilon} = \underline{u}_0' + \underline{u}' - \underline{\underline{R}}\,\bar{\imath}_1, \tag{9}$$

where $\underline{u}_0$ is the position vector of the beam's axis in its reference configuration. The strain vector is defined as $\underline{\varepsilon}^T = \left\{\varepsilon_{11}, \gamma_{12}, \gamma_{13}\right\}$, where ε_{11} is the sectional axial strain, and γ_{12} and γ_{13} the two components of transverse shearing strains.

In the GEBF, the interpolation of the displacement field takes the following form,

$$\underline{u}(s) = h_1(s)\underline{\hat{u}}^{(1)} + h_2(s)\underline{\hat{u}}^{(2)} + h_3(s)\underline{\hat{u}}^{(3)} + h_4(s)\underline{\hat{u}}^{(4)}, \tag{10a}$$

$$\phi(s) = h_1(s)\hat{\phi}^{(1)} + h_2(s)\hat{\phi}^{(2)} + h_3(s)\hat{\phi}^{(3)} + h_4(s)\hat{\phi}^{(4)}, \tag{10b}$$

where $s \in [-1, +1]$ is a non-dimensional variable along the span of the element, as indicated in fig. 3. As depicted in fig. 3, the interpolation is based on the nodal values of the displacement vector, denoted $\underline{\hat{u}}^{(i)}$ at nodes $i = 1, 2, 3, 4$ and of the cross-sectional rotation, denoted $\hat{\phi}^{(i)}$ at nodes $i = 1, 2, 3, 4$. The shape functions of the element are defined as follows [30],

$$\begin{aligned} h_1(s) &= \frac{9}{16}(s^2 - \frac{1}{9})(1 - s), \quad h_3(s) = -\frac{27}{16}(1 - s^2)(s - \frac{1}{3}), \\ h_2(s) &= \frac{9}{16}(s^2 - \frac{1}{9})(1 + s), \quad h_4(s) = \frac{27}{16}(1 - s^2)(s + \frac{1}{3}). \end{aligned} \tag{11}$$

Rational techniques for the interpolation of finite rotations have been proposed by numerous authors [31, 32].

At this point, it is worth pointing out fundamental differences between the ANCF and GEBF formulations. Because second derivatives appear in the ANCF curvature-displacement relationship, see eq. (1), C_1 continuity is required at inter-element boundaries [10, 11]. The strain-displacement relationships for GEBF involve first derivatives only, see eqs. (6) and (9), and hence, C_0 continuity only is required. Consequently, ANCF uses Hermitian polynomial shape functions, eq. (4), to interpolate position and slope vectors and achieve C_1 continuity. The nodal variables are the positions and slopes at the ends of the two-node element; higher-order elements can be formulated. On the other hand, GEBF uses Lagrangian shape functions, eq. (11), to interpolate the displacement and rotation fields independently, leading to C_0 continuity for both. The nodal variables are the displacements and rotations at the nodes; both end-point and internal nodes are used. These considerations have a profound impact on the discretization process used in the two approaches and explain the differences illustrated in fig. 3.

2.4 The strain energy

The strain energy stored in the planar deformation of a shear deformable beam [18] of length L is expressed as

$$\begin{aligned} A = &\frac{1}{2}\int_0^L H\kappa^2(\alpha_1)\,\mathrm{d}\alpha_1 \\ &+ \frac{1}{2}\int_0^L S\varepsilon^2(\alpha_1)\,\mathrm{d}\alpha_1 + \frac{1}{2}\int_0^L K\gamma^2(\alpha_1)\,\mathrm{d}\alpha_1, \end{aligned} \tag{12}$$

where H is the bending stiffness, S the axial stiffness, and K the shearing stiffness. The beam's deformation is characterized by three sectional strain measures: the curvature, $\kappa(\alpha_1)$, the axial strain, $\varepsilon(\alpha_1)$, and the transverse shear strain, $\gamma(\alpha_1)$.

The properties of the beam are assumed to remain constant along its span and it will be convenient to use a non-dimensional expression for the strain energy

$$\bar{A} = \frac{1}{2}\int_0^1 \bar{\kappa}^2(\eta)\ \mathrm{d}\eta + \frac{1}{2}\frac{1}{\bar{a}^2}\int_0^1 \varepsilon^2(\eta)\ \mathrm{d}\eta + \frac{1}{2}\frac{1}{\bar{s}^2}\int_0^1 \gamma^2(\eta)\ \mathrm{d}\eta, \tag{13}$$

where $\bar{A} = LA/H$ is the non-dimensional strain energy, $\bar{\kappa} = L\kappa$ the non-dimensional curvature, and $\eta = \alpha_1/L$ the non-dimensional span-wise variable along the beam's span. Two non-dimensional stiffness parameters have been defined,

$$\bar{a}^2 = \frac{H}{SL^2} = \frac{1}{12}\left(\frac{h}{L}\right)^2, \tag{14a}$$

$$\bar{s}^2 = \frac{H}{KL^2} = \frac{1}{10}\left(\frac{E}{G}\right)\left(\frac{h}{L}\right)^2. \tag{14b}$$

The axial stiffness coefficient, denoted $\bar{a}^2$, is the ratio of the bending to the axial stiffness of the beam, and the shear stiffness coefficient, denoted $\bar{s}^2$, is the ratio of the bending to the shear stiffness of the beam. The second equalities in eqs. (14) hold for homogeneous beams presenting a rectangular cross-section of width b and height h, and made of a homogeneous material of Young's modulus E and shear modulus G.

The non-dimensional expression of the strain energy presented in eq. (13) reveals some of the inherent difficulties associated with the solution of beam problems. For long, slender beams, the axial and shear stiffness coefficients both become very small as $(h/L)^2 \to 0$. The axial and shear energies, represented by the second and third terms in eq. (13), respectively, decrease rapidly because $\varepsilon \to 0$ and $\gamma \to 0$, respectively; hence, the axial and shear energies have little effect on the solution. At the same time, the coefficients multiplying the last two integrals in eq. (13) become large, $1/\bar{a}^2 \to \infty$ and $1/\bar{s}^2 \to \infty$.

The behavior described in the previous paragraph is often called "naturally occurring penalty formulation." Coefficients $1/\bar{a}^2$ and $1/\bar{s}^2$ can be viewed as large penalty coefficients that enforce constraints $\varepsilon \approx 0$ and $\gamma \approx 0$, respectively. In numerical implementations, if the discretization of the displacement field does not allow the axial and shear strain vanish, the last two integrals in eq. (13) cannot vanish, leading to membrane and shear locking, respectively.

3 Planar beam subjected to bending moments

Figure 2 depicts a straight, uniform beam of length $2L$ subjected to end concentrated bending moments, Q. For this simple two-dimensional problem, an exact solution [18] of the problem is available: the beam deforms into a circle of radius R, as shown in the figure. The curvature and radius of curvature are constant along the beam's span and in non-dimensional form, they are

$$\bar{\kappa}(\eta) = \frac{L}{R}, \quad \text{and} \quad \bar{\varrho}(\eta) = \frac{R}{L}, \tag{15}$$

respectively. Of course, both axial and shear strain components vanish for this pure bending problem.

For the ANCF, the exact solution of the problem is written in terms of the position of the deformed reference line,

$$\bar{x}_1 = \sin\theta, \quad \bar{x}_2 = 1 - \cos\theta, \tag{16}$$

where $\bar{x}_1 = \alpha_1/R$ and $\bar{x}_2 = x_2/R$ are the non-dimensional components of the position vector of the beam's reference line. Equation (16) is the parametric equation of a circle, since the beam's reference line does deform into a circle exactly. It is verified easily that the axial strain component given by eq. (2) vanishes for the position field given in eqs. (16).

For the GEBF, the exact solution of the problem is written in terms of the displacement field of the beam's reference axis and of the rotation field of the cross-section

$$\bar{u}_1 = \sin\theta - \theta, \quad \bar{u}_2 = 1 - \cos\theta, \quad \phi = \theta, \tag{17}$$

where $\bar{u}_1 = u_1/R$ and $\bar{u}_2 = u_2/R$ are the non-dimensional components of the displacement vector of a point of the reference axis of the beam and ϕ the rotation of its cross-section. Equation (17) is the displacement field for the initially straight beam deforming into a circle. It is verified easily that axial and shear strain components given by eqs. (9) vanish for the displacement field given in eqs. (17).

3.1 First assessment: kinematic solution

The previous section has presented the exact solution of a planar bending problem. Since the solution is known, exact nodal solutions are found easily; the solutions predicted by the ANCF and GEBF inside the elements will then be compared. To obtain a fair comparison between the two approaches, different meshes were used for the two formulation: the ANCF uses two, two-noded elements totaling twelve degrees of freedom and the GEBF uses one, four-noded element involving the same number of degrees of freedom.

3.1.1 Exact nodal solutions

For the ANCF, the exact nodal solutions at nodes 2 and 3, see fig. 2, are found easily

$$\bar{x}_1^{(2)} = \sin\bar{\kappa}, \quad \bar{x}_2^{(2)} = 1 - \cos\bar{\kappa}, \quad \bar{r}_1^{(2)} = \bar{\kappa}\cos\bar{\kappa}, \quad \bar{r}_2^{(2)} = \bar{\kappa}\sin\bar{\kappa}, \tag{18a}$$

$$\bar{x}_1^{(3)} = 0, \qquad \bar{x}_2^{(3)} = 0, \qquad \bar{r}_1^{(3)} = \bar{\kappa}, \qquad \bar{r}_2^{(3)} = 0. \tag{18b}$$

The solution at node 1 is found be replacing $\bar{\kappa}$ by $-\bar{\kappa}$ in the solution for node 3.

For the GEBF, the exact nodal solutions at nodes 2 and 4, see fig. 2, are found easily

$$\bar{u}_1^{(2)} = \sin\bar{\kappa} \quad - \bar{\kappa} \quad , \quad \bar{u}_2^{(2)} = 1 - \cos\bar{\kappa} \quad , \quad \phi^{(2)} = \bar{\kappa} \quad , \tag{19a}$$

$$\bar{u}_1^{(4)} = \sin\bar{\kappa}/3 - \bar{\kappa}/3, \quad \bar{u}_2^{(4)} = 1 - \cos\bar{\kappa}/3, \quad \phi^{(4)} = \bar{\kappa}/3, \tag{19b}$$

The solutions at node 1 and 3 are found be replacing $\bar{\kappa}$ by $-\bar{\kappa}$ in the above equations.

3.1.2 First assessment: numerical results

Given the exact nodal solution for the GEBF and ANCF stated in eqs. (19) and (18), respectively, the displacement and strain fields can be evaluated at any point within the element using the shape functions and their spatial derivatives. The interpolated curvature, axial strain, and shear strain fields denoted κ_a, ϵ_a, and γ_a, respectively, were compared to their exact counterpart, denoted κ_e, $\epsilon_e = 0$, and $\gamma_e = 0$, respectively. The following error measures were selected for these three

quantities

$$e_\kappa = \sqrt{\frac{1}{N_{gp}} \sum_{k=1}^{N_{gp}} \left(\frac{\kappa_a(s_k) - \kappa_e(s_k)}{\kappa_e(s_k)} \right)^2}, \tag{20a}$$

$$e_\epsilon = \sqrt{\frac{1}{N_{gp}} \sum_{k=1}^{N_{gp}} \epsilon_a^2(s_k)}, \tag{20b}$$

$$e_\gamma = \sqrt{\frac{1}{N_{gp}} \sum_{k=1}^{N_{gp}} \gamma_a^2(s_k)}. \tag{20c}$$

All quantities were evaluated at N_{gp} sampling points denoted s_k. Within each element, 3 sampling points were selected to coincide with the location of the Gauss-Legendre quadrature points within the element.

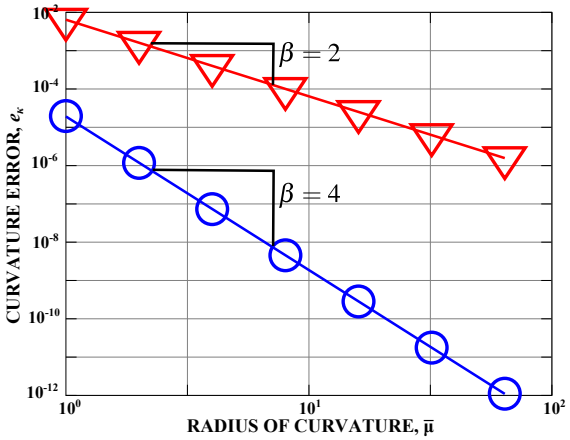

Figure 4: Curvature error measure defined by eq. (20a) versus non-dimensional radius of curvature, $\bar{\mu}$. ANCF: $\bigtriangledown$; GEBF: $\bigcirc$.

To assess the accuracy of the two approaches, the curvature error defined by eq. (20a) was computed for an increasing number of elements, 1, 2, 4, 8, 16, 32, and 64. As the number of elements increases, the radius of curvature divided by the element size increases, and the accuracy of the curvature interpolation increases. To measure the convergence rate of the two approaches, the error measure defined by eq. (20a) is plotted versus the radius of curvature divided by the element size, denoted $\bar{\mu}$; a logarithmic scale is used in the plot. Figure 4 shows the results of the computation with symbols $\bigtriangledown$ and $\bigcirc$ for the ANCF and GEBF predictions, respectively. Linear regression of the numerical data was performed to assess the convergence rate. Because logarithmic scales are used, this linear regression is of the following form, $\log e_\kappa = \alpha - \beta \log \bar{\mu}$, where coefficient β is a measure of the convergence rate; higher values of this coefficient indicate a higher convergence rate. Figure 4 shows that $\beta = 2$ and 4 for the ANCF and GEBF, respectively. Clearly, the curvature field predicted by GEBF is far more accurate than that predicted by ANCF.

Figure 5 shows the corresponding results for the axial strain field. In this case, coefficient $\beta = 4$ for both ANCF and GEBF, and the predictions of the ANCF are slightly more accurate than those of the GEBF. Finally, fig. 6 depicts the shear strain error for the GEBF, for which $\beta = 3$; of course, the ANCF predicts a vanishing shear strain, as expected.

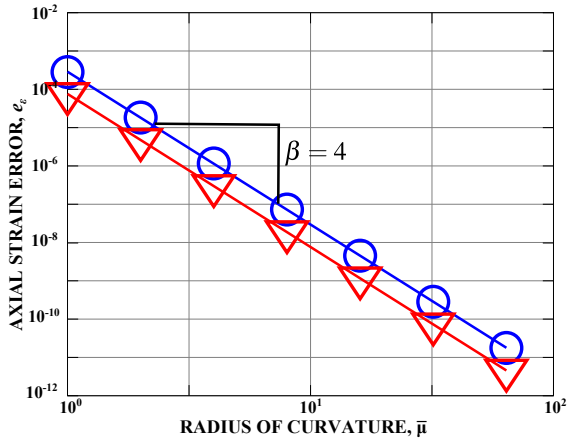

Figure 5: Axial strain error measure defined by eq. (20b) versus non-dimensional radius of curvature, $\bar{\mu}$. ANCF: $\bigtriangledown$; GEBF: $\bigcirc$.

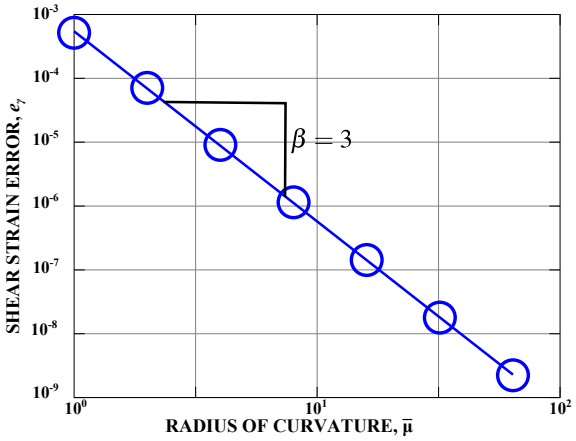

Figure 6: Shear strain error measure defined by eq. (20c) versus non-dimensional radius of curvature, $\bar{\mu}$. GEBF: $\bigcirc$.

3.2 Second assessment: static solution

In the previous section, the exact solution of the planar bending problem depicted in fig. 2 was imposed at the nodes and the accuracy of the interpolated solution was investigated. In practice, the exact solution is not known but computed with the help of the principle of virtual work. This approach is followed in this second assessment. Due to the symmetry of the problem, the right half of the system was modeled only; the beam was clamped at point **O** and a bending moment, Q, was applied at the beam's tip. In the exact solution, the beam's curvature is constant along its span and the non-dimensional curvature is $\bar{\kappa} = QL/H$, where H is the beam's bending stiffness. Here again, a single cubic element was used for the GEBF and two cubic elements were used for the ANCF; in both cases, three Gauss points were used to evaluated the stiffness matrices.

In contrast with the kinematic solution presented in the previous section, the static solution does not predict the exact solution at the nodes. For instance, the predicted displacement and rotation at point **T** indicated on fig. 2 are no longer exact. The tip displacement error measure is selected as $e_u = \|\underline{u}_a^T - \underline{u}_e^T\|/\|\underline{u}_e^T\|$, where $\underline{u}_a^T$ and $\underline{u}_e^T$ are the predicted and exact displacement vectors at point **T**, respectively. Similarly, the tip rotation error measure is selected as $e_\phi = |\phi_a^T - \phi_e^T|/|\phi_e^T|$, where ϕ_a^T and ϕ_e^T are the predicted and exact cross-sectional rotations at point **T**, respectively. Figures 7 and 8 shows the error measures for tip displacement and rotation, respectively, versus the non-dimensional radius of curvature, $\bar{\rho}$, together with the linear regression. Convergence of the GEBF is indicated by $\beta = 5.7$ and 6.0 for the tip displacement and rotation errors, respectively.

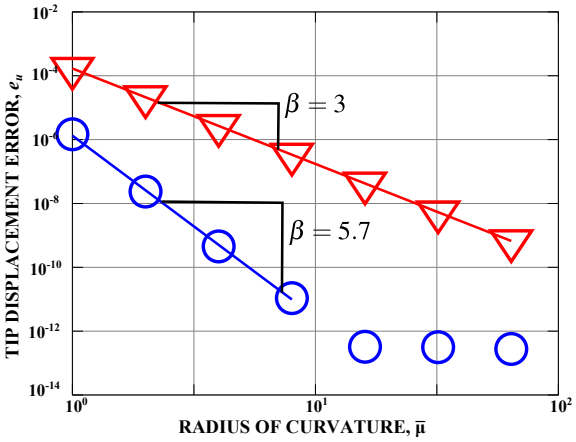

Figure 7: Tip displacement error measure, $e_u = \|\underline{u}_a^T - \underline{u}_e^T\|/\|\underline{u}_e^T\|$, versus non-dimensional radius of curvature, $\bar{\mu}$. ANCF: $\bigtriangledown$; GEBF: $\bigcirc$.

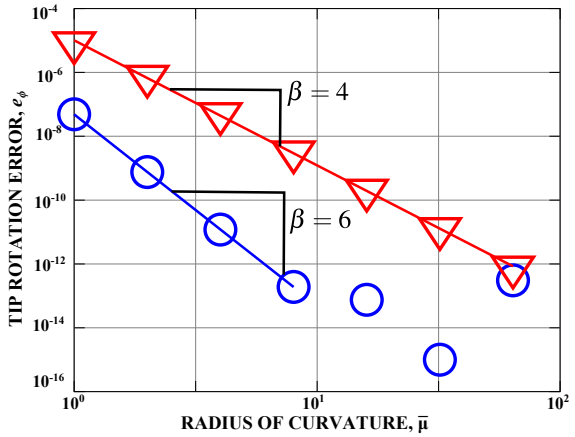

Figure 8: Tip rotation error measure, $e_\phi = |\phi_a^T - \phi_e^T|/|\phi_e^T|$, versus non-dimensional radius of curvature, $\bar{\mu}$. ANCF: $\bigtriangledown$; GEBF: $\bigcirc$.

The corresponding ANCF predictions are far less accurate with $\beta = 3$ and 4 for the same quantities, respectively.

Next, fig. 9 shows the error measure for the curvature defined by eqs. (20a) versus the non-dimensional radius of curvature, $\bar{\rho}$, for the static solution using both ANCF and GEBF. The results of the GEBF are almost exact, within the numerical accuracy of the solution procedure. It is interesting to compare the results shown in figs. 4 and 9; clearly, the static solution yields more accurate predictions than the kinematic solution. In contrast, the ANCF predictions are less accurate and furthermore, a cursory look at figs. 4 and 9 reveals that the kinematic and static solutions are of comparable accuracy, with $\beta = 2$ in both cases.

Next, fig. 10 shows the error measure for the axial strain defined by eqs. (20b) versus the non-dimensional radius of curvature, $\bar{\rho}$, for the static solution using both ANCF and GEBF. Here again, the predictions of the GEBF are nearly exact, and the static solution is more accurate than its kinematic counterpart, as observed by comparing figs. 5 and 10. In contrast, the ANCF predictions are less accurate and furthermore, a cursory look at figs. 5 and 10 reveals that the kinematic and static solutions are nearly of the same level of accuracy, with $\beta = 4$ for both cases.

Figure 11 shows the error measure for the shear strain defined by eqs. (20c) versus the non-dimensional radius of curvature, $\bar{\rho}$, for the static solution using GEBF. As observed for the case of the axial strains, the predictions of the GEBF are nearly exact. Of course, for the ANCF, the shear strains vanish exactly.

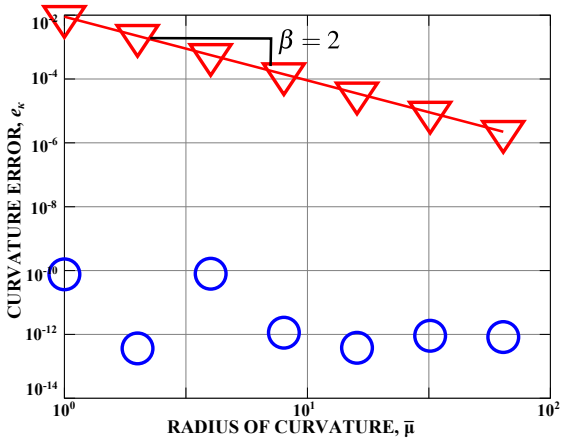

Figure 9: Curvature error measure defined by eq. (20a) versus non-dimensional radius of curvature, $\bar{\mu}$. ANCF (2GP): $\bigtriangledown$; GEBF: $\bigcirc$.

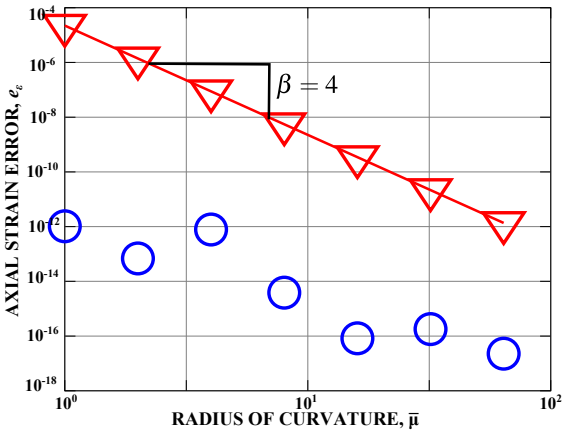

Figure 10: Axial strain error measure defined by eq. (20c) versus non-dimensional radius of curvature, $\bar{\mu}$. ANCF: $\bigtriangledown$; GEBF: $\bigcirc$.

For the GEBF, predictions obtained from the static solution are more accurate than those obtained from the kinematic solution. This stems from the fact that the static solution is based on the principle of virtual work, which averages errors over the beam's span to obtain the best possible solution in an energy norm. To demonstrate this effect, fig. 12 shows the curvature field error, $L\kappa(s) - \bar{\kappa}$, along the beam's span for both kinematic and static solutions. Also indicated on the figure are the locations of the Gauss points used in the integration of the stiffness matrix. For the static solution, the curvature distribution shifts so as to minimize the errors at the Gauss points. For the case depicted in fig. 12, the error measures defined by eq. (20a) are $e_\kappa = 1.96\ 10^{-5}$ and $e_\kappa = 7.60\ 10^{-11}$ for the kinematic and static solutions, respectively.

In case of the GEBF, fig. 13 shows the corresponding results for the axial and shear strain distributions along the beam's span. The error measures for axial strains, defined by eq. (20b), are $e_\varepsilon = 2.81\ 10^{-4}$ and $e_\varepsilon = 1.03\ 10^{-12}$ for the kinematic and static solutions, respectively. For the shear strain, the corresponding errors, defined by eq. (20c), are $e_\gamma = 5.17\ 10^{-4}$ and $e_\gamma = 2.76\ 10^{-11}$ for the kinematic and static solutions, respectively.

In contrast, the accuracy of the static solution provided by the ANCF is not markedly better than that of its kinematic counterpart. Figure 14 shows the curvature field error, $L\kappa(s) - \bar{\kappa}$, along the beams's span for both kinematic and static solutions. Also indicated on the figure are the locations of the Gauss points used in the integration of the stiffness matrix. The accuracies of kinematic and static solutions are comparable. For the case depicted in fig. 14, the error measures

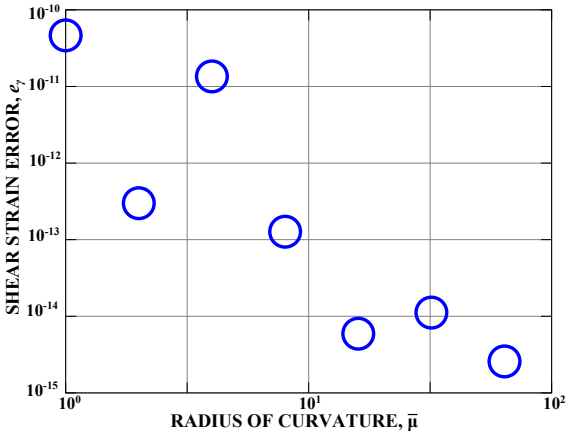

Figure 11: Shear strain error measure defined by eq. (20c) versus non-dimensional radius of curvature, $\bar{\mu}$. GEBF: ◯.

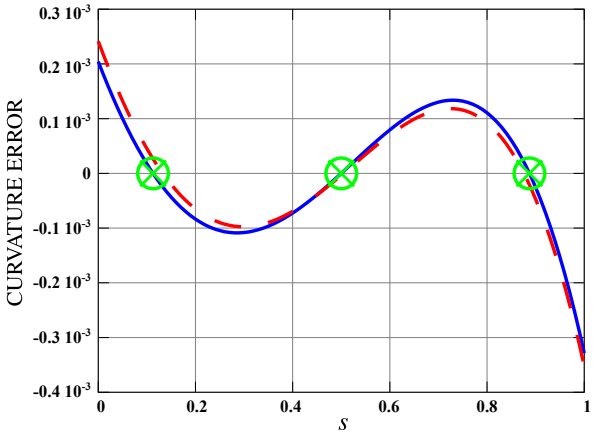

Figure 12: Curvature distribution along the beam's span. Kinematic solution: dashed line; static analysis: solid line. $\bar{\varrho} = 1$. The locations of the Gauss points are indicated by symbols ⊗.

defined by eq. (20a) are $e_\kappa = 6.44\ 10^{-3}$ and $e_\kappa = 8.82\ 10^{-3}$ for the kinematic and static solutions, respectively.

Figure 15 shows the corresponding results for the axial strain distribution along the beam's span. The error measures for axial strains defined by eq. (20b) are $e_\varepsilon = 7.55\ 10^{-5}$ and $e_\varepsilon = 2.20\ 10^{-5}$ for the kinematic and static solutions, respectively.

Table 1: ANCF predictions for beams with two aspect ratios, $\bar{h} = 1/10$ and $1/1000$.

$\bar{h}$	$1/\bar{a}^2$	$1/\bar{s}^2$	e_ϕ	e_ϵ	e_γ	e_κ
1 / 10	$1.20\ 10^3$	$3.85\ 10^2$	$8.27\ 10^{-6}$	$2.20\ 10^{-5}$	0	$8.82\ 10^{-3}$
1 / 1000	$1.20\ 10^7$	$3.85\ 10^6$	$6.02\ 10^{-5}$	$2.21\ 10^{-9}$	0	$8.87\ 10^{-3}$

As mentioned earlier, the formulation of beam elements involves "naturally occurring penalty terms" and hence, membrane and shear locking are likely to occur. To study the potential occurrence of locking, two beam configurations were studied featuring aspect ratios $\bar{h} = h/L = 1/10$ and $1/1000$. In both cases, the beam was subjected to a tip bending moment resulting in $\bar{\rho} = 1$. Table 1 lists the errors in the beam's tip rotation and the strain components at the 3 Gauss points for the two aspects ratios, when using the ANCF; the corresponding results obtained from the GEBF appear in table 2.

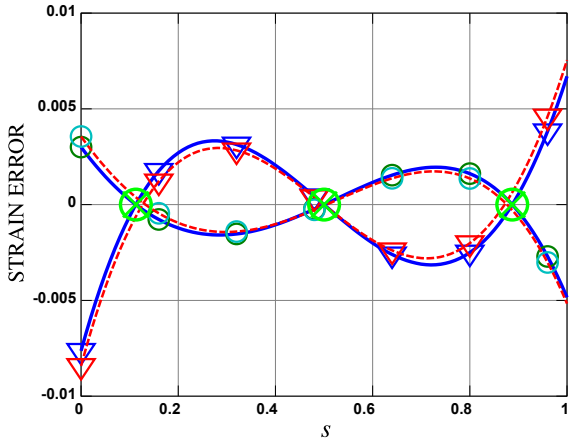

Figure 13: Axial (◯) and shear (▽) strain distributions along the beam's span. Kinematic solution: dashed line; static solution: solid line. $\bar{\varrho} = 1$, $\bar{h} = 1/10$. The locations of the Gauss points are indicated by symbols ⊗.

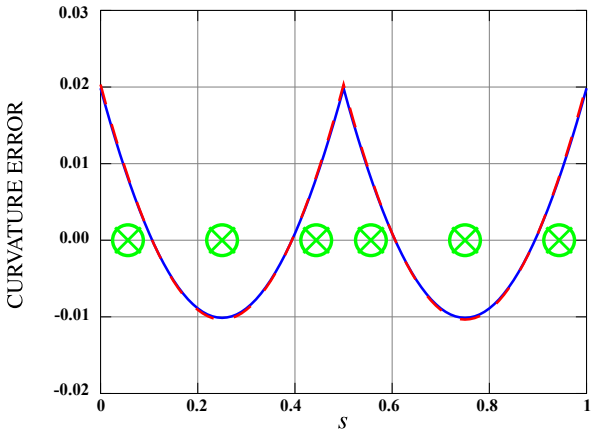

Figure 14: Curvature distribution along the beam's span. Kinematic solution: dashed line; static solution: solid line. $\bar{\varrho} = 1$. The locations of the Gauss points are indicated by symbols ⊗.

4 Discussion

The results presented in the previous section contrast the performance of the ANCF and GEBF applied to simple planar beam problems. Both kinematic and static solutions were discussed.

In the kinematic solution, the exact nodal displacements were prescribed and the predicted displacement and strain fields inside the element were compared for the ANCF and GEBF. The accuracies of the predicted strain fields were found to be markedly different for the two approaches. While the accuracies of the axial strain fields were comparable, see fig. 5, those of the curvature fields differed sharply, see fig. 4. The kinematic solution involves the kinematic characteristics of the two formulations only: the definition of the strain-displacement relationships and the selection of the shape functions. The expression of the strain energy and the definition of the elastic forces play no role in this procedure. Because cubic shape functions are used in both formulations, the

Table 2: GEBF predictions for beams with two aspect ratios, $\bar{h} = 1/10$ and $1/1000$.

$\bar{h}$	$1/\bar{a}^2$	$1/\bar{s}^2$	e_ϕ	e_ϵ	e_γ	e_κ
1 / 10	$1.20\ 10^3$	$3.85\ 10^2$	$4.86\ 10^{-8}$	$1.03\ 10^{-12}$	$4.65\ 10^{-11}$	$7.60\ 10^{-11}$
1 / 1000	$1.20\ 10^7$	$3.85\ 10^6$	$4.86\ 10^{-8}$	$8.17\ 10^{-14}$	$1.60\ 10^{-13}$	$4.76\ 10^{-13}$

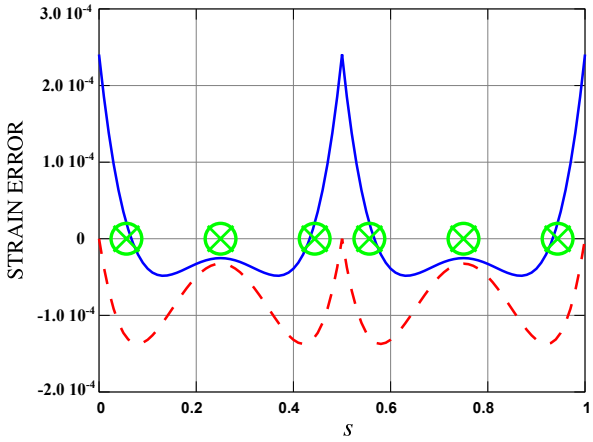

Figure 15: Axial strain distributions along the beam's span. Kinematic solution: dashed line; static solution: solid line. $\bar{\varrho} = 1$, $\bar{h} = 1/10$. The locations of the Gauss points are indicated by symbols $\otimes$.

observed difference in accuracy is likely to stem from the different strain-displacement relationships used in the two formulations.

Indeed, in the ANCF, the curvature field is evaluated as a *second* derivative of the displacement field, see eq. (1), whereas the same curvature field is obtained from a *first* derivative of the displacement field in the GEBF, see eq. (6). The interpolated displacement field is inherently approximate; hence, taking successive derivatives of this interpolated field to evaluate strain components further deteriorates accuracy. Clearly, the GEBF predicts a more accurate curvature field because this field is obtained as a *first* derivative of displacements, whereas the accuracy of the ANCF is inherently lower because curvatures are evaluated as *second* derivatives of the displacement field.

This observation also explains the different continuity requirements at inter-element boundaries [10, 11]: because second derivatives appear in the ANCF strain-displacement relationships, C_1 continuity is required at inter-element boundaries, whereas C_0 continuity only is required for GEBF. These more stringent continuity requirements for ANCF elements imply that special procedures must be used when connecting neighboring elements presenting slope discontinuities, as discussed by Shabana *et al.* [33, 34, 35]. In contrast, the lower continuity requirements for GEBF elements imply a greater ease of use, specially when complex model of realistic multibody systems must be developed.

In the static solution, rather than prescribing exact nodal displacements, the principle of virtual work was used to compute the solution of a simple planar beam problem based on the ANCF and GEBF. In this procedure, errors over the beam's span are averaged to obtain the best possible solution in an energy norm [10, 11]. Because Gaussian integration was used to evaluate the elastic forces and stiffness matrices in both ANCF and GEBF, this averaging process is based on Gauss point information, and the predictions of both formulations were compared at these points.

Here again, a sharp difference was observed between the two formulations. For the GEBF, the accuracy of the predictions improved markedly when going from the kinematic to the static solution procedure. On the other hand, no improvement was observed for the ANCF: the errors observed for the kinematic and static solution procedures are of the same order of magnitude. This finding echoes similar observations by Romero [17], who documented the higher computational cost of ANCF as compared to GEBF. Figures 14 and 15 provide an explanation of this phenomenon: the distributions of curvature and axial strain errors are even functions of local variable s defined in fig 3. Consequently, it is difficult to minimize the error at the three (odd number) Gauss points. In contrast, figs. 12 and 13 show that the corresponding error distributions for the GEBF are odd functions of variable s that nearly vanish at the Gauss points. Accuracy does not improve

for the ANCF when using two or four Gauss points. Given the strain-displacement relationships used by ANCF, the axial and bending strain distributions along the length of each ANCF element are described by polynomials of different order, which cannot vanish, or nearly vanish, at the same points. Consequently, when repeating ANCF simulations with 2, 3, and 4 Gauss points, similar accuracies were observed; the best accuracy was obtained with the three Gauss point scheme reported here.

5 Conclusions

This paper has presented a detailed comparison between the ANCF and GEBF used for flexible multibody dynamics. A brief review of the two formulations underscored a fundamental difference in the strain-displacement relationships used by the two methods. Next, a simple planar beam problem was used to contrast the predictions of the ANCF and GEBF for both kinematic and static solutions.

In the kinematic solution, the exact nodal displacements were prescribed and the predicted displacement and strain fields inside the element were compared for the two methods. The accuracies of the predicted strain fields were found to differ markedly: the predictions of the GEBF were more accurate than those of the ANCF. This phenomenon can be explained by the fact that the curvature field is obtained as a second derivative of the displacement in the ANCF, but as a first derivative only for the GEBF. For the static solution, the principle of virtual work was used to determine the solution of the problem. For the GEBF, the predictions of the static solution are far more accurate than those obtained from the kinematic solution; in contrast, the same order of accuracy is obtained for the two solution procedures when using ANCF.

It appears that the kinematic description of beam problems offered by the ANCF leads to inherently lower accuracy predictions than those provided by the GEBF. In the ANCF, the curvature description uses second derivatives of the displacements, impacting the performance of ANCF adversely. First, taking successive derivatives of the displacement field degrades accuracy, because of the approximate nature of the interpolation for the displacement field. Secondly, the strain-displacement relationships yield axial and bending strain distributions along the length of each element that are of different polynomial orders, making it difficult to minimize integration error when evaluating element force and stiffness characteristics.

While the present paper has focused on beam elements, plate and shell elements based on the ANCF will suffer similar drawbacks because in those elements, curvatures are also evaluated based on second derivatives of the displacement field. Note that textbooks detailing the fundamentals of the finite element method [10, 11, 36] recommend to use the lowest possible order of derivative in the strain-displacement relationships of structural mechanics elements; higher-order derivatives lead to lower accuracy and higher continuity requirements at inter-element boundaries.

References

[1] P. Eberhard and W. Schiehlen. Computational dynamics of multibody systems: History, formalisms, and applications. *Journal of Computational and Nonlinear Dynamics*, 1(1):3–12, January 2006.

[2] T.M. Wasfy and A.K. Noor. Computational strategies for flexible multibody systems. *ASME Applied Mechanics Reviews*, 56(2):553–613, 2003.

[3] A.A. Shabana and R.A. Wehage. A coordinate reduction technique for dynamic analysis of spatial substructures with large angular rotations. *Journal of Structural Mechanics*, 11(3):401–431, March 1983.

[4] O.P. Agrawal and A.A. Shabana. Application of deformable-body mean axis to flexible multibody system dynamics. *Computer Methods in Applied Mechanics and Engineering*, 56(2):217–245, 1986.

[5] A.A. Shabana. Flexible multibody dynamics: Review of past and recent developments. *Multibody System Dynamics*, 1(2):189–222, June 1997.

[6] J.C. Simo. A finite strain beam formulation. The three-dimensional dynamic problem. Part I. *Computer Methods in Applied Mechanics and Engineering*, 49(1):55–70, 1985.

[7] A.A. Shabana, H.A. Hussien, and J.L. Escalona. Application of the absolute nodal coordinate formulation to large rotation and large deformation problems. *ASME Journal of Mechanical Design*, 120:188–195, 1998.

[8] J. Gerstmayr, H. Sugiyama, and A. Mikkola. An overview on the developments of the absolute nodal coordinate formulation. In *Proceedings of the Second Joint International Conference on Multibody System Dynamics*, Stuttgart, Germany, May 2012.

[9] M. Géradin and A. Cardona. *Flexible Multibody System: A Finite Element Approach*. John Wiley & Sons, New York, 2001.

[10] T.J.R. Hughes. *The Finite Element Method*. Prentice Hall, Inc., Englewood Cliffs, New Jersey, 1987.

[11] K.J. Bathe. *Finite Element Procedures*. Prentice Hall, Inc., Englewood Cliffs, New Jersey, 1996.

[12] J.C. Simo and L. Vu-Quoc. A three-dimensional finite strain rod model. Part II: Computational aspects. *Computer Methods in Applied Mechanics and Engineering*, 58(1):79–116, 1986.

[13] M. Borri and T. Merlini. A large displacement formulation for anisotropic beam analysis. *Meccanica*, 21:30–37, 1986.

[14] D.A. Danielson and D.H. Hodges. Nonlinear beam kinematics by decomposition of the rotation tensor. *Journal of Applied Mechanics*, 54(2):258–262, 1987.

[15] D.A. Danielson and D.H. Hodges. A beam theory for large global rotation, moderate local rotation, and small strain. *Journal of Applied Mechanics*, 55(1):179–184, 1988.

[16] A.A. Shabana. Definition of the slopes and the finite element absolute nodal coordinate formulation. *Multibody System Dynamics*, 1:339–348, 1997.

[17] I. Romero. A comparison of finite elements for nonlinear beams: the absolute nodal coordinate and geometrically exact formulations. *Multibody System Dynamics*, 20:51–68, 2008.

[18] O.A. Bauchau and J.I. Craig. *Structural Analysis with Application to Aerospace Structures*. Springer, Dordrecht, Heidelberg, London, New-York, 2009.

[19] S.P. Timoshenko. On the correction factor for shear of the differential equation for transverse vibrations of bars of uniform cross-section. *Philosophical Magazine*, 41:744–746, 1921.

[20] S.P. Timoshenko. On the transverse vibrations of bars of uniform cross-section. *Philosophical Magazine*, 43:125–131, 1921.

[21] E. Reissner. The effect of transverse shear deformation on the bending of elastic plates. *Zeitschrift für angewandte Mathematik und Physik*, 12:A.69–A.77, 1945.

[22] R.D. Mindlin. Influence of rotatory inertia and shear on flexural motions of isotropic elastic plates. *Journal of Applied Mechanics*, 18:31–38, 1951.

[23] E. Reissner. On one-dimensional finite-strain beam theory: the plane problem. *Zeitschrift für angewandte Mathematik und Physik*, 23:795–804, 1972.

[24] E. Reissner. On one-dimensional large-displacement finite-strain beam theory. *Studies in Applied Mathematics*, 52:87–95, 1973.

[25] E. Reissner. On finite deformations of space-curved beams. *Zeitschrift für angewandte Mathematik und Physik*, 32:734–744, 1981.

[26] L.E. Malvern. *Introduction to the Mechanics of a Continuous Medium*. Prentice Hall, Inc., Englewood Cliffs, New Jersey, 1969.

[27] J. Gerstmayr and H. Irschik. On the correct representation of bending and axial deformation in the absolute nodal coordinate formulation with an elastic line approach. *Journal of Sound and Vibration*, 318(3):461–487, 2008.

[28] A.A. Shabana and R.Y. Yakoub. Three dimensional absolute nodal coordinate formulation for beam elements: Theory. *ASME Journal of Mechanical Design*, 123:606–613, 2001.

[29] R.Y. Yakoub and A.A. Shabana. Three dimensional absolute nodal coordinate formulation for beam elements: Implementation and applications. *ASME Journal of Mechanical Design*, 123:614–621, 2001.

[30] O.A. Bauchau. *Flexible Multibody Dynamics*. Springer, Dordrecht, Heidelberg, London, New-York, 2011.

[31] M.A. Crisfield and G. Jelenić. Objectivity of strain measures in the geometrically exact three-dimensional beam theory and its finite-element implementation. *Proceedings of the Royal Society, London: Mathematical, Physical and Engineering Sciences*, 455(1983):1125–1147, 1999.

[32] O.A. Bauchau and S.L. Han. Interpolation of rotation and motion. *Multibody System Dynamics*, 31(3):339–370, 2014.

[33] A.A. Shabana and A.M. Mikkola. Use of the finite element absolute nodal coordinate formulation in modeling slope discontinuity. *ASME Journal of Mechanical Design*, 125(2):342–350, 2003.

[34] A.A. Shabana and L.G. Maqueda. Slope discontinuities in the finite element absolute nodal coordinate formulation: Gradient deficient elements. *Multibody System Dynamics*, 20:239–249, 2008.

[35] L.G. Maqueda and A.A. Shabana. Numerical investigation of the slope discontinuities in large deformation finite element formulations. *Nonlinear Dynamics*, 58:23–37, 2009.

[36] O.C. Zienkiewicz, R.L. Taylor, and J.Z. Zhu. *The Finite Element Method: Its Basis and Fundamentals*. Elsevier, Butterworth Heinemann, Amsterdam, sixth edition, 2005.